Multiscale Characterisation Study on the Effect of Heat Treatment on the Microstructure of Additively Manufactured 316L Stainless Steel

Benjamin Jenkins, Auriane Etienne, Eric Baustert, Gregory Rose, Cristelle Pareige, Philippe Pareige, Bertrand Radiguet

Multiscale Characterisation Study on the Effect of Heat Treatment on the Microstructure of Additively Manufactured 316L Stainless Steel

Authors: Benjamin M. Jenkins[1], Auriane Etienne[1], Eric Baustert[2], Gregory Rose[2], Cristelle Pareige[1], Philippe Pareige[1], Bertrand Radiguet[1]

1) Univ Rouen Normandie, CNRS, INSA Rouen Normandie, Groupe de Physique des Matériaux UMR 6634, F-76000 Rouen, France

2) Volum-e, 1 Chemin de la Fonderie, 76340 Blangy-sur-Bresle, France

Corresponding author: benjamin.jenkins@univ-rouen.fr

Keywords
Additive manufacture, austenitic stainless steel, microstructure, heat treatment, electron microscopy, atom probe tomography, characterisation

Abstract
Additively manufactured 316L components are known to exhibit complex three-dimensional microstructures on multiple length-scales. The effect of heat treatment on the stability of grains and dislocation cell structures within the microstructure has previously been investigated but there are appreciable disagreements surrounding the nature of the texture that is present in the specimens, and there is also limited published work on the compositional homogeneity of specimens, particularly on the atomic scale, after heat treatments.

In this study, we investigate the effect of applying two different heat treatments to 316L components produced by laser powder bed fusion before characterising them using a combination of electron microscopy and atom probe tomography. The importance of using multiple characterisation techniques, which span from the nanometre to micrometre scale, in addition to carefully and accurately describing analysis methods when investigating the evolution of the microstructure of additively manufactured 316L steels is demonstrated.

Our EBSD (Electron Back Scatter Diffraction) results show the presence of a strong <110> texture in the build direction of the samples, and a reduction in morphological texture as a result of heat treatment. TEM (Transmission Electron Microscopy) results indicate a dissolution of the dislocation cell structure that forms during solidification. Atom probe tomography was used to investigate compositional homogeneity in the samples and indicated that there are regions enriched in Cr, Mn, Mo, and Ni in the As-Printed samples that are likely associated with the dislocation cell walls. The atom probe results also reveal the presence of impurities, such as Co, which were not detected in the feedstock powder.

1. Introduction
Austenitic stainless steels, such as 316L, are commonly used for reactor internals in the primary circuit of light water nuclear power plants (NPPs) due to their good creep resistance, adequate mechanical properties at elevated temperatures and their satisfactory corrosion resistance [1]. Austenitic steels are also proposed for use in fusion reactors [2] and several advanced fission reactor designs [3].

Many of the components made from 316L in NPPs are complex in shape and require multistep manufacturing processes. Additive manufacture (AM) offers the opportunity to create net-shape components without the need for further machining; this is beneficial as it will reduce material waste and may also decrease manufacturing time and cost for bespoke components [4–6].

AM has two primary potential applications within the nuclear industry. Firstly, AM could be used to manufacture components in currently operational NPPs that need replacing but are no longer commercially produced. This may lead to the extension of the safe operational lifetime of ageing NPPs. Secondly, advanced reactor designs may rely on more complex component geometries and AM may be able to produce prototypes of these components more readily and at reduced cost than conventional processing methods.

However, highly complex microstructures across multiple length scales arise due to the rapid heating and cooling experienced during AM processing [7–13]. The development of a morphological and crystallographic texture during printing is well known in FCC materials, although there is disagreement as to whether a <110> or <100> type crystallographic texture dominates in the building direction [10,13–21]. Since many authors incompletely describe how their Electron Back Scatter Diffraction (EBSD) data was analysed, it is difficult to conclude from the literature whether this difference in build direction texture is due to different printing parameters, or if it is a result of differences in data collection and analysis methods. One critical factor, which is often not reported when analysing crystallographic texture within EBSD data, is the choice of the direction for the inverse pole figure (IPF) when compared to the reference coordinates of the sample [22]. Without this important information it is not possible to verify in which direction crystallographic texture is present within samples presented in the literature.

Post-printing heat treatments can be applied to relieve internal stresses and to homogenise the microstructure of AM 316L components so that it is similar to wrought components [23]. However, this process adds to the manufacturing time and has an associated economic cost that is related to the duration and temperature of the applied heat treatment. Studying the effect of post-printing heat treatments on the microstructure and chemical homogeneity within specimens is essential for determining if a heat treatment process will provide a satisfactory microstructure and mechanical properties to the materials [14,15,24–26].

In this paper, additively manufactured 316L samples subjected to two different post-print heat treatments are characterised using electron microscopy and atom probe tomography. The combination of techniques permits the structure and chemical distribution within the samples to be studied from the micro- to the nano-scale and to be compared to an as-printed sample that underwent no form of heat treatment. The importance of selecting suitable atom probe experimental conditions and carefully describing EBSD data analysis decisions is discussed at-length, and it is hoped that this article represents a guide as to how to employ characterisation techniques that span several length scales to accurately characterise microstructural changes in additively manufactured alloys subjected to various heat treatments. It may also help to explain the origin of the differences in crystallographic texture that are frequently reported in the literature.

2. Materials and Methods

The investigated materials were additively manufactured using laser powder bed fusion (LPBF) with an EOS M 290 machine. Samples of size 10 mm x 10 mm x 15 mm were printed using a feedstock powder provided by EOS that was sampled according to ASTM B215 and had the composition given in Table 1. The nominal composition was determined

using a combination of inductively coupled plasma optical emission spectroscopy and combustion and fusion-based chemical evaluation methods.

Table 1: Nominal composition (wt.%) of 316L powder used as feedstock to manufacture samples.

Element	Fe	Cr	Ni	Mo	Mn	Si	Cu	N	C	P
Wt.%	63.39-64.77	17.12 - 17.72	13.30 - 14.03	2.64 - 2.82	1.55 - 1.68	0.35	0.03 - 0.04	0.07 - 0.08	0.02	0.009 - 0.013

The printing parameters employed to create the samples are presented in Table 2. A rotation of 67˚ was applied to the laser scan direction for each successive layer. The selected parameters are widely used in the AM industry and produce components with properties that meet the requirements of ASTM F3184-16.

Table 2: Parameters used during additive manufacture process of samples.

Parameter	Value Used
Average powder size (diameter)	50 µm
Layer thickness	40 µm
Sample size	10 mm x 10 mm x 15 mm
Laser spot size (diameter)	80 µm
Pressure and gas in chamber	0.7 bar of Argon
Core laser power	200-250 W
Core laser speed	900-1000 mm/s
Hatch Size	170 µm
Building Platform temperature	80°C
Energy input	55 J/mm^3 - 60 J/mm^3

After printing, one sample received a solution annealing heat treatment of 1150 ˚C for 90 minutes followed by quenching in water whilst a second sample was heat treated at 1066 ˚C for 75 minutes before being slow-cooled at 10 ˚C/minute in argon gas. Henceforth, these will be referred to as “1150 ˚C HT” and “1066 ˚C HT”, respectively. A third sample received no post-printing heat treatment and will henceforth be referred to as “As-Printed”. The heat treatment temperatures were selected since, at both temperatures, only austenite and the $MnCr_2O_4$ spinel should be present in the equilibrium microstructure [15] and they should therefore both be suitable for generating a recrystallised microstructure.

Due to the complex microstructural features that arise on a range of length scales from additive manufacturing of metallic powders, it was necessary to use multiple techniques to perform characterisation across a series of different length scales. Electron backscatter diffraction (EBSD), transmission electron microscopy (TEM), and atom probe tomography (APT) were used. Prior to EBSD characterisation, each sample was sectioned such that the internal microstructure could be examined in the planes parallel and perpendicular to the build direction (Figure 1). Each surface underwent mechanical grinding and polishing in order to minimise any surface damage, with a final diamond suspension of size 0.1 µm used.

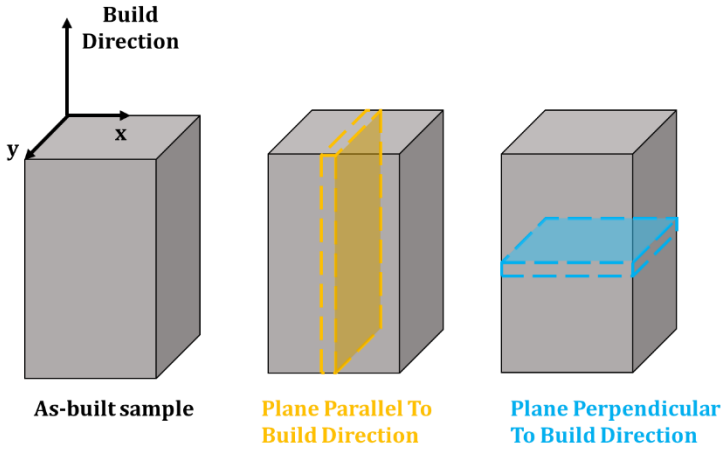

Figure 1 Schematic diagram showing the different surfaces studied and their relationship to the build direction of the sample.

2.1 Electron Backscatter Diffraction

Electron backscatter diffraction was performed using a JEOL 7900F scanning electron microscope equipped with an EDAX Hikari Super EBSD Camera and EDAX APEX EBSD v2.5.1 software. Accelerating voltages of 20 kV, currents of 1 nA – 2 nA, and spot sizes of 0.5 µm and 1 µm were used. Post processing of the EBSD data was performed using EDAX OIM Analysis v8.5.1002 with Neighbor CI Correlation was used to "cleanup" EBSD data. Multiple EBSD scans were performed on each sample, with each individual scan covering an area larger than ~ 0.25 mm^2.

2.2 Focused Ion Beam Sample Preparation

Focused ion beam (FIB) was used to prepare TEM and APT samples. Standard procedures using dual-beam FIB/SEMs - including a Zeiss XB-540 and a FEI Gallium Helios 5 UX - were followed for preparing TEM foils [27] and APT needles [28–31]. After FIB thinning, a Gatan Precision Ion Polishing System II (PIPS II) was used for final thinning of the TEM samples and to also remove any FIB-induced surface damage [32] using 0.5 keV Ar^+ ions. A final FIB polishing stage was carried out on the APT specimens at 2 kV to minimise Ga^+ implantation into the analysed volumes [31].

2.3 Transmission Electron Microscopy

Transmission electron microscopy (TEM) and Scanning TEM (STEM) analysis was conducted using a double corrected (probe and image CEOS correctors) JEOL-ARM200CF microscope, equipped with a cold field emission gun (FEG) and operating at 200 kV. Energy Dispersive Spectroscopy (EDS) was carried out using a single JEOL Centurio EDS 2300T silicon drift detector (SDD) with Analysis Station v 3.8 software. The solid collection angle for the EDS detector is 1 steradian (sr).

2.4 Atom Probe Tomography

Atom probe tomography (APT) specimens were analysed with a LEAP 5000XR in the GENESIS facility. Whilst the majority of experiments were conducted in voltage-pulsing mode, some others were conducted in laser-pulsing mode so that the effect of analysis conditions on data quality could be investigated. For voltage-mode experiments, a pulse fraction of 20 % was used, whilst the laser energy for individual laser-pulsing experiments was set between 20 pJ and 80 pJ so that the effect of varying laser pulse energy could be investigated. Analysis temperatures varied between 50 K – 60 K. A pulse frequency of 200

kHz was used for all experiments but detection rates varied between 0.002 and 0.005 ions per pulse.

Reconstructions were performed using Cameca's integrated visualisation and analysis software (IVAS) 3.8.16. Compositional calculations were performed using AtomProbeLab due to its ability solve peak overlaps within the mass spectra and to quantify compositional measurement uncertainty [33,34]. Further analyses, including image generation, were performed using GPM 3DSAT software
(CNRS IDDN: IDDN.FR.001.430017.000.S.P.2020.000.10000).

3. Results & Discussion

3.1 Electron Backscatter Diffraction

EBSD maps for the As-Printed, 1066 ˚C HT, and 1150 ˚C HT samples are presented in Figure 2. The building direction is indicated for each micrograph. The inverse pole figure (IPF) has been orientated parallel to the building direction so that crystallographic texture in this direction can be visualised in the IPF maps and further investigated.

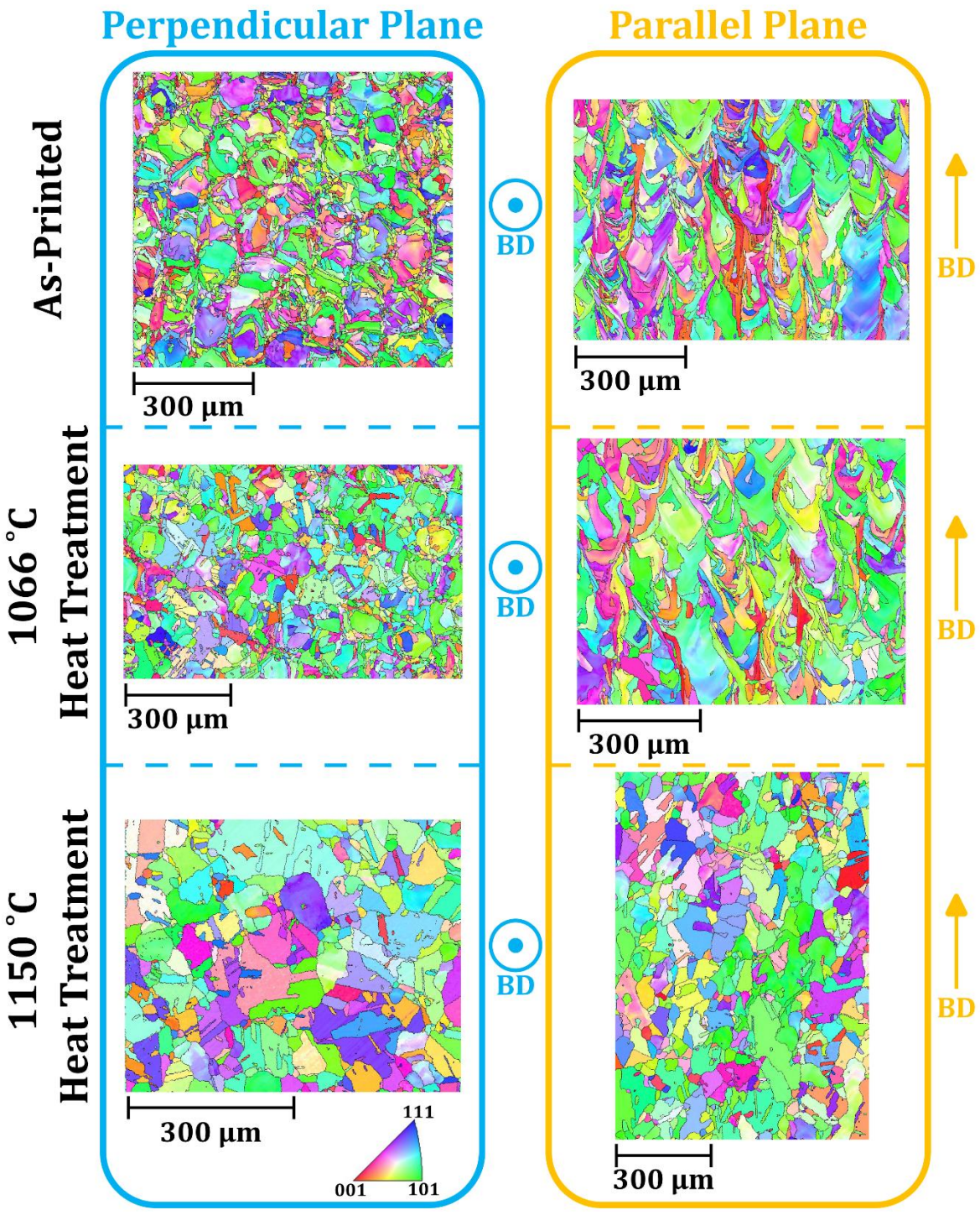

Figure 2 EBSD maps for the three samples analysed in this study. The IPF direction is along the building direction such that the crystallographic texture in these directions can be seen. BD indicates the build/printing direction of the samples.

3.1.2 Crystallographic Texture

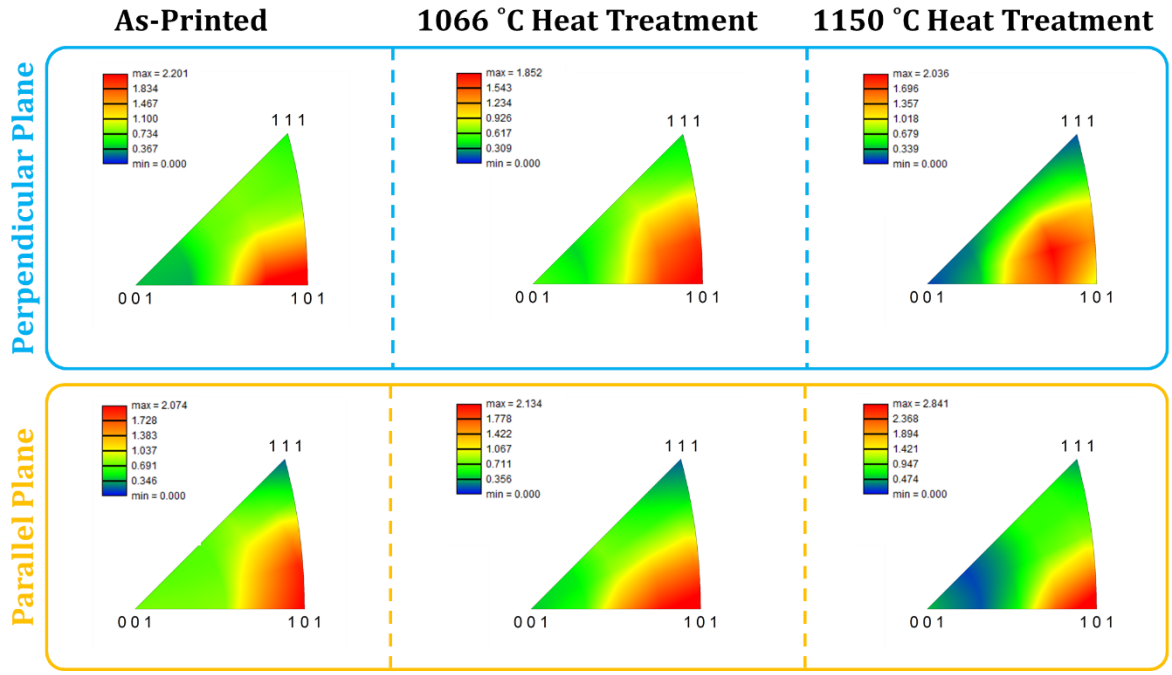

Figure 3 Corresponding inverse pole figures for the maps in Figure 2, showing the dominant crystallographic direction in the building direction for each of the samples.

The As-Printed sample has a <110> texture in the building direction. This crystallographic texture strengthens after applying heat treatments at 1066 ˚C or 1150 ˚C (Figure 2 and Figure 3), which is consistent with previous work by Kong et al. [35].

Whilst some studies report the absence of any crystallographic texture in additively manufactured FCC materials [35–41], the presence of a microscopic crystallographic texture is frequently described elsewhere in the literature. However, the preferred orientation of this crystallographic texture is sometimes reported as strongly favoured <110> with respect to the building direction [10,13–17,42–51], whilst others state the dominance of a <100> texture in the building direction [18–21,52–57]. The source of the discrepancy between <100> and <110> growth dominating in the building direction has been rationalised as arising due to the implementation of different parameters during the printing process [21,42,48,49,58–60]. During the solidification of FCC metals, growth of <100> orientated grains along the maximum heat flow direction will dominate [60]. Since the variation of printing process parameters will impact the magnitude of thermal gradients, and their orientation with respect to the building and laser scanning direction, the direction of <100> dominant growth within the samples will vary as a result. This can lead to the development of a {110}<001> Goss texture along the laser scan direction [16,17]. Sun et al. state that “a long, shallow melt pool promotes the formation of <001> texture, whereas a short, deep melt pool favours the occurrence of <011> texture” in the building direction [49].

However, a major difficulty in interpreting the relationship between build direction and crystallographic texture is that published literature often fails to specify the relationship between the IPF direction and the build direction of specimens, despite the known importance of accurately defining the sample reference frame when studying crystallographic texture [22]. This is particularly pertinent when studying additively manufactured specimens, since different crystallographic textures may arise in different directions within the sample due to varying heating and cooling profiles in the laser scan and build directions. In order to correctly identify the crystallographic texture in the building direction it is necessary to examine IPF maps with the IPF direction orientated in the building direction of the

specimens. Figure 4 demonstrates the effect of changing the IPF direction on the observed crystallographic texture in the 1066 ˚C HT sample. It can be seen that orientating the IPF direction along the specimen build direction leads to the identification of a <101> type crystallographic texture. Meanwhile, if the IPF direction is orientated in the specimen x or specimen y direction, <111> and <001> crystallographic textures are more apparent. This highlights the critical importance of correctly orientating the IPF when performing crystallographic texture analyses in AM materials, and of reporting this orientation with respect to the sample coordinates.

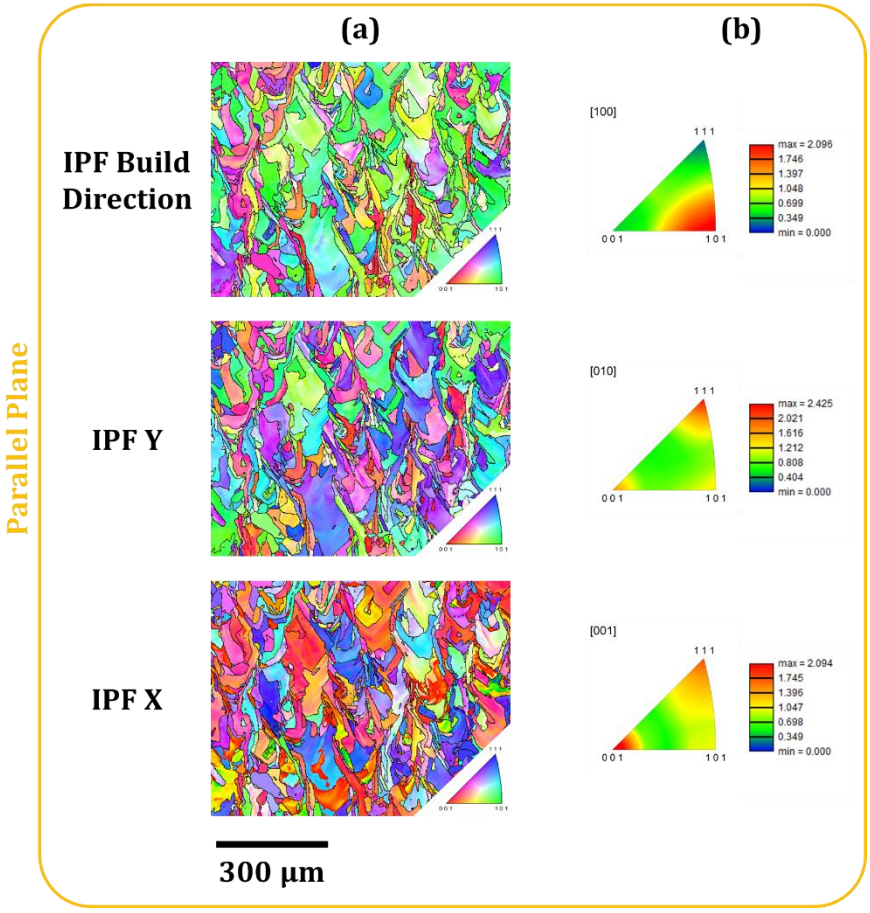

Figure 4 Effect of changing IPF direction on apparent crystallographic texture for 1066 ˚C HT sample (map plane parallel to build direction). (a) IPF orientation maps and (b) Inverse pole figures showing the distribution of crystallographic orientations in each of the maps from (a).

3.1.1 Morphological Changes After Heat Treatment

In the plane perpendicular to the build direction, circular regions with an average diameter of 85 µm ± 10 µm can be seen in the As-Printed sample (Figure 2). These features are less visible after the heat treatment at 1066 ˚C and cannot be discerned after the 1150 ˚C heat treatment. Both applied heat treatments are above the recrystallisation temperature of 316L, with recrystallisation in additively manufactured 316L samples previously observed above 1000 ˚C [15], and twins are clearly visible in the microstructure of the heat-treated samples (Figure 2). The fraction of recrystallised grains is expected to increase at longer heat treatment times, with more than 90 % of the sample recrystallised observed after 500 minutes heat treatment at 1150 ˚C compared to around 45 % after 15 minutes of ageing at the same temperature [13].

In the As-Printed and 1066 ˚C HT samples, melt pools are visible in the plane parallel to the building direction. These melt pools are no longer present after the 1150 ˚C heat treatment, although there is a preference for grains to be elongated in the build direction in the 1150 ˚C HT sample (Figure 5 (a)). This morphological texture suggests that the melt pools influence grain growth during heat treatment. Previously, applying a heat treatment at 1150 ˚C for 2 hours was observed to lead to a "more isotropic configuration" of grains, although there was no discussion of any relationship between their major axis and the building direction [23]. Our results in Figure 2 and Figure 5 (a) indicate that the grains are indeed elongated in the build direction after heat treatment at 1150 ˚C; the average aspect ratio between the minor and major axis is around 0.5, indicating that grains are approximately twice as long in the build direction as they are in the transverse directions (Figure 5 (b)). The inhomogeneity of grain size in different orientations within the sample is likely to lead to anisotropic mechanical properties, such as a lower tensile strength in the building direction.

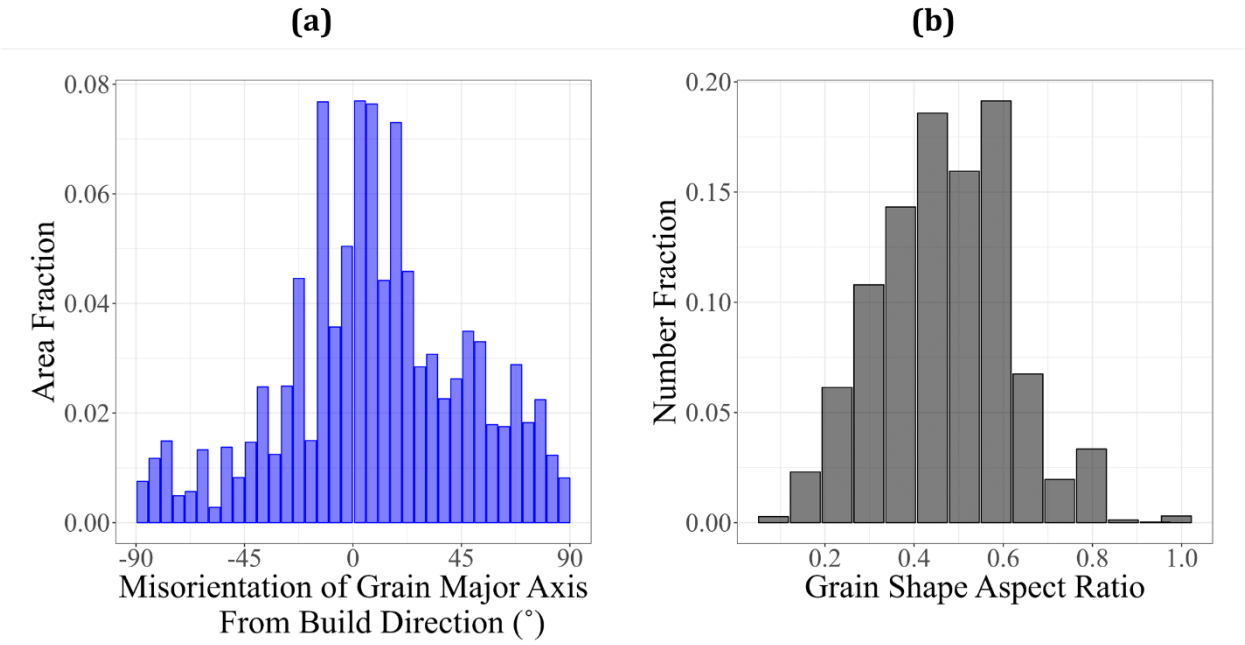

Figure 5 (a) Distribution of the grain major axis orientations and (b) Grain shape aspect ratio between length of minor and major axes for grains in the plane parallel to the building direction for the 1150 ˚C heat-treated sample. N.B. 0˚ of orientation indicates major grain axis is aligned with build direction of the sample.

3.2 Transmission Electron Microscopy

Dendrites and dislocation cell structures are commonly observed in additively manufactured materials. The high density of dislocations at the cell walls is believed to arise due to residual stresses that occur during thermal expansion/shrinkage during solidification [12,61,62]. Figure 6 shows the presence of dislocation cell structures in the As-Printed sample. The cells were 400 nm – 500 nm in width and segregation of Mn, Cr, and Mo to the cell boundaries was observed, which is consistent with studies on other additively manufactured austenitic stainless steels [37,38,61,62]. Quantitative STEM-EDS analysis indicated that Cr, Mn, and Mo were present in higher concentrations in the cell walls, as shown in Table 3. Figure 6 shows that the Mn-enrichment at the boundaries was less uniform than that of Cr and Mo. The segregation of Si to the boundaries was not strongly visible in the STEM-EDS data, although there are some small circular regions of higher silicon intensity associated with triple points between the cells as indicated by the arrows and

circles in Figure 6 (g); similar local regions of enrichment have been previously observed [37]. The micrographs in Figure 6 were taken along a [100] zone axis and it is reasonable to assume the alignment of the cells along the <100> directions as has been shown by Berstch et al. [61].

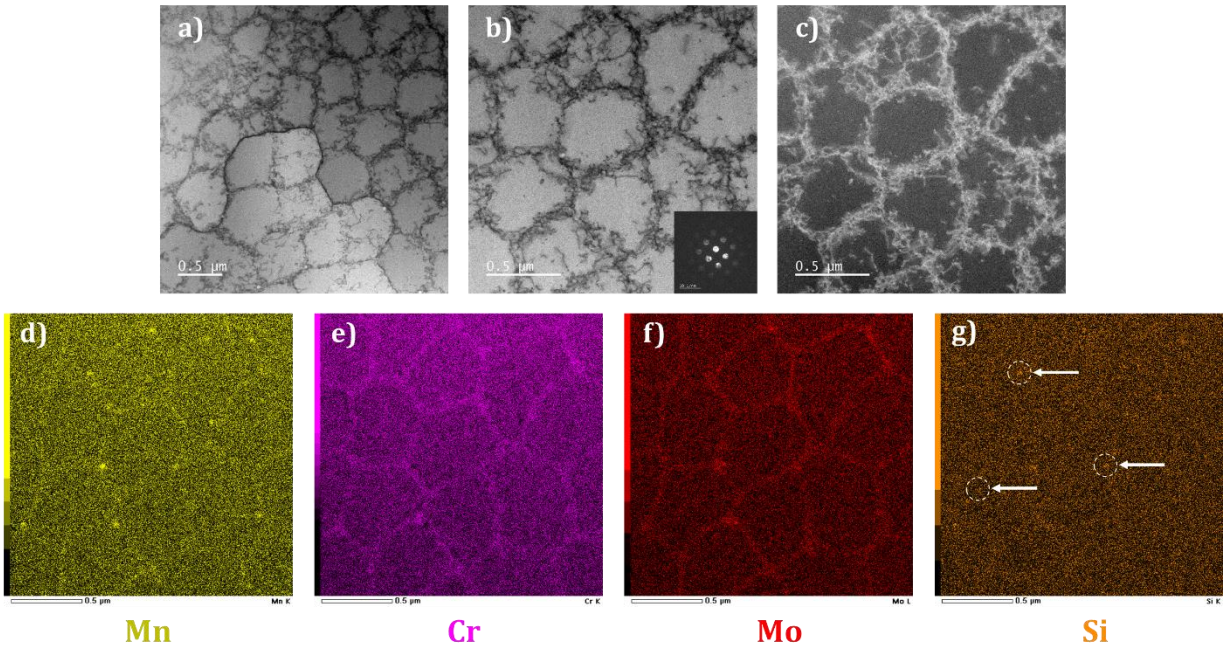

Figure 6 (a) and (b) Bright-field and (c) LAADF STEM images of dislocation cell structures in the As-Printed sample. STEM-EDS maps show segregation of (d) Mn (e) Cr (f) Mo and (g) Si to the cell boundaries in (b) and (c). Images were collected on the [001] zone axis with a probe size of 6C and a camera length of 8 cm. The electron current for the EDS maps was 15.2 µA.

Table 3 STEM-EDS composition (at.%) of the cell cores and the cell walls in the As-Printed sample.

Element	Cell Core (at.%)	Cell Wall (at.%)
Cr	18.1 ± 0.1	18.9 ± 0.1
Fe	62.9 ± 0.0	61.3 ± 0.1
Mn	1.7 ± 0.0	1.8 ± 0.0
Mo	2.1 ± 0.0	2.6 ± 0.0
Ni	14.6 ± 0.1	14.7 ± 0.0
Si	0.5 ± 0.0	0.5 ± 0.0

TEM investigations of the 1066 ˚C HT and 1150 ˚C HT samples revealed that the dendrite cell structure was no longer present and STEM-EDS maps indicated that the solutes did not segregate to any linear features (Supplementary Figure 1). This is consistent with previous reports that state the cellular microstructure is stable up to 873 K (600 ˚C) [39], and disappears entirely at higher annealing temperatures [35,63,64].

3.3 Atom Probe Tomography

Multiple APT analyses were conducted for each specimen. All elements were randomly distributed within the APT volumes for each of the three samples, as shown by the atom maps in Figure 7. It is important to note that APT samples volumes are very small compared to the size of the specimens and also to the areas that can be mapped by STEM-EDS.

The fact that no segregation was observed in individual As-Printed APT samples does not necessarily mean that no cell walls were analysed via APT or that there is no segregation of certain elements to the cell walls, as has been previously reported [56]. Chen et al. conducted correlative TEM/APT and observed no segregation in their APT data, although they also observed no segregation to the cell walls in their STEM-EDS data [56].

Indeed, the lack of segregation detected within individual APT datasets in this study could be due to multiple factors. Firstly, the APT volumes in the As-Printed specimen may have only sampled volumes from within the cell cores, as has been observed within additively manufactured Ni alloys [65] and would be unsurprising given that the STEM-EDS data in Figure 6 indicates that the cell walls make up a small fraction of the total sample volume. Secondly, it could be that the segregation of elements to the cell walls is fairly diffuse on the length-scale of APT and is not highly concentrated versus the composition of the matrix; for example, Figure 6 shows that there is some element enrichment at the cell walls, but this enrichment is not particularly strong and appears diffuse over 50 – 100 nm, which is on the same order of size as an entire APT volume.

To investigate which of the above options was most likely, the composition of individual datasets in the As-Printed samples was investigated and compared to the compositions of the heat-treated datasets. The vast majority of datasets had very similar compositions with one another. However, there were some As-Printed datasets that had slightly higher levels of Cr, Mn, V, and Mo within them (Figure 8), and we propose that it is likely that these datasets sampled a cell wall or a region near to one. Interestingly, the distribution of elements within these datasets appeared to be uniform, indicating that the enrichment of segregating elements at cells walls may be quite diffuse. Whilst the measured composition of the cell cores and cell walls are slightly different to those measured by STEM-EDS (Table 3), the trend for Mo, Cr, and Mn enrichment is consistent between both techniques.

When the average composition of the remaining As-Printed APT datasets, which we assume are the cell interiors, was compared to the heat-treated samples, it is interesting to note that the compositional measurement information presented in Figure 8 indicates there is no appreciable difference in the average measured compositions. Since STEM-EDS observes the dissolution of the cell structure after heat treatment and the redistribution of solute elements, it may be expected that the heat-treated samples analysed by APT would contain higher levels of Ni, Mo, and Si than the APT analyses of the cell cores in the As-Printed samples. However, the small volume fraction of the cell walls in the sample and the only slight enrichment of elements at them may explain why this is not observed.

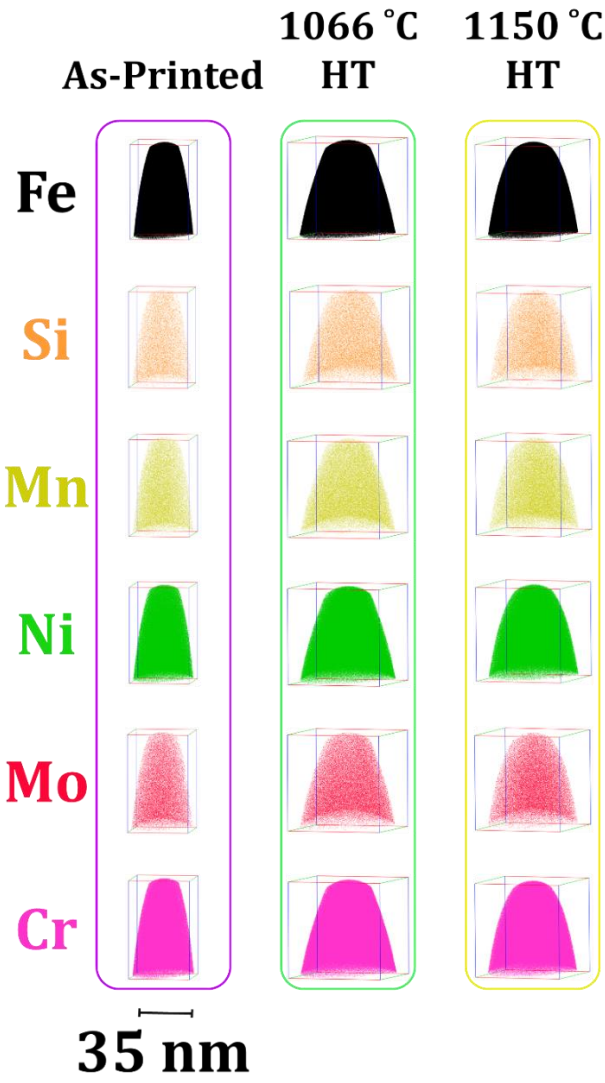

Figure 7 Representative atom maps showing the random distribution of Fe, Si, Mn, Ni, Mo, and Cr atoms in the As-Printed, 1066 ˚C HT and 1150 ˚C HT samples.

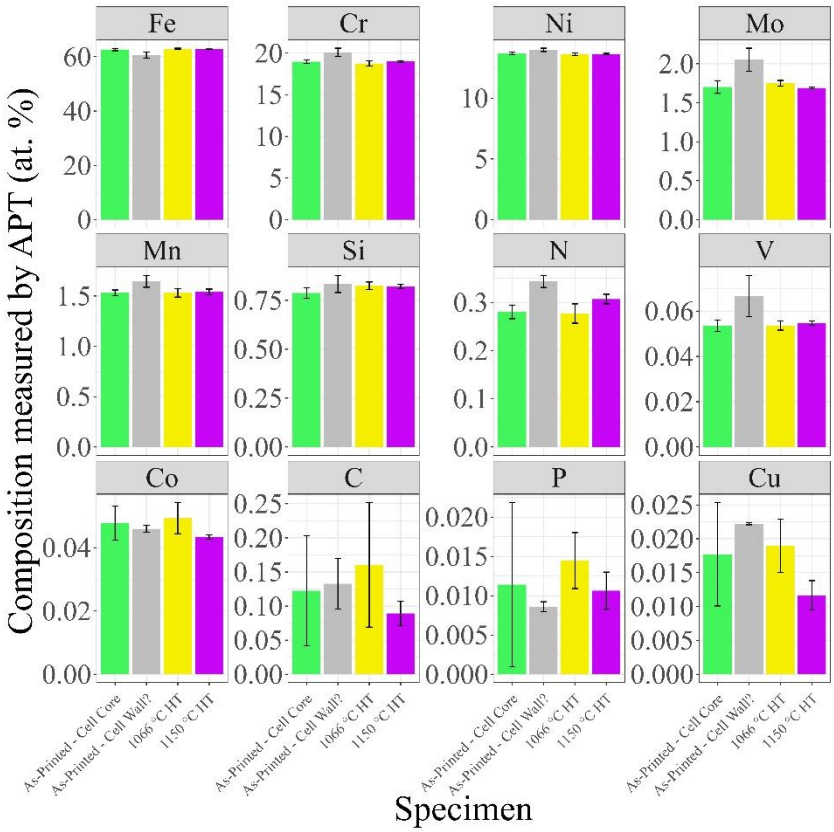

Figure 8 Plot showing how the mean composition measured by APT varies between the As-Printed – Cell Core and Cell Wall, 1066 ˚C HT and 1150 ˚C HT samples. N.B. only voltage-mode experiments performed at or below 55 K were included in these compositional analyses.

Co was detected in all the volumes analysed by APT. The presence of Co is notable despite the fact that it is in low concentration and is unlikely to have any major impact on the mechanical properties of the additively manufactured components. Co is known to transmute into ^{60}Co as a result of exposure to neutrons. ^{60}Co has high radiation activity levels after exposure to neutrons and, whilst it is present as an impurity in many alloys used in the nuclear industry, the IAEA state that levels of Co should be minimised [66]. Since some additively manufactured 316L components are proposed for use in the nuclear industry, it is important that the Co levels within them are known and controlled and that the origin of the Co is known. The APT results here demonstrate the importance of testing for Co within the feedstock powder when it is sampled prior to the manufacture of components, and also in ensuring that LPBF units that are used to print multiple alloys are thoroughly cleaned between each batch to avoid Co contamination.

3.3.1 Effect of Analysis Conditions

The effect of APT analysis conditions on the quality of the data was investigated by varying the operating temperature, laser pulsing energy, and using voltage-pulsing mode. No surface migration [67] of any species was observed in voltage-pulsing mode whilst using laser energies of 20 pJ was found to lead to the surface migration of P and Si atoms to crystallographic poles. Figure 9 shows that the magnitude of this effect increased with increasing laser pulse energy, which is consistent with the results of Hyde et al. when analysing ferritic reactor pressure vessel steels [68]. Therefore the use of laser mode, especially at higher laser energies, will reduce the spatial resolution of APT when studying the distribution of Si and P atoms in 316L steels and should be avoided where possible.

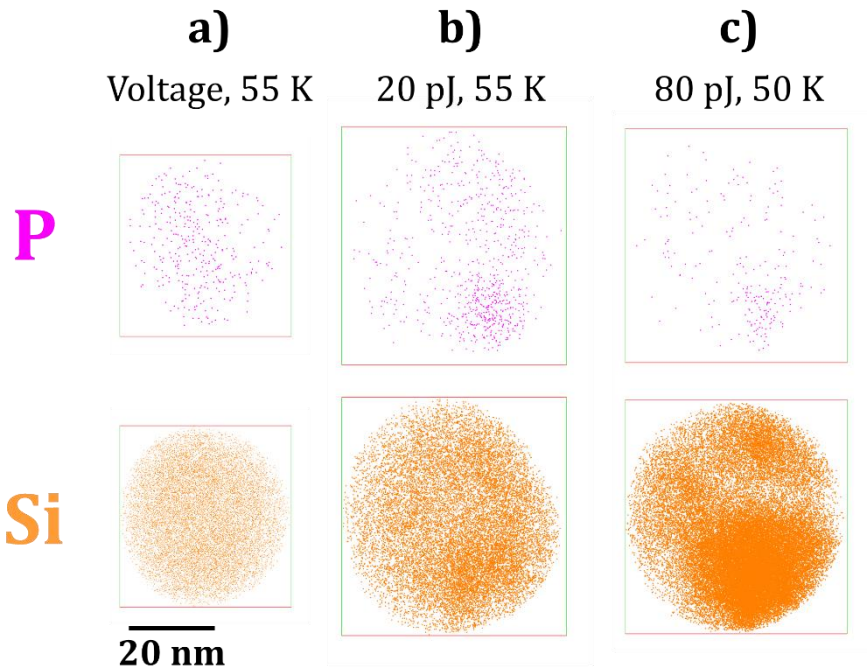

Figure 9 Increased surface migration of Si and P observed in the As-Printed sample with increasing laser energy from a) voltage pulsing at 55 K to b) laser pulsing 20 pJ at 55 K to c) laser pusling 80 pJ at 50 K.

4. Conclusions

The results presented here demonstrate the importance of employing a range of characterisation techniques across multiple length-scales in order to observe the complex three-dimensional structures that arise in additively manufactured materials, and to study their evolution under different heat treatments. For each technique used, it is crucial that users are aware of how analysis conditions and data analysis decisions can impact their observations. Specifically, APT data should be acquired under a range of experimental conditions to determine which are most suitable, and variations in measurements between datasets should be carefully interpreted. Meanwhile, EBSD data must always be presented and described with reference to co-ordinate system of the printing direction – this is of particular significance when performing texture analyses with respect to the printing or laser scan directions in AM alloys.

Our EBSD results showed that applying heat treatment at higher temperature led to a greater reduction in the morphological texture of the components, with melt pools and features due to the powders/laser spot becoming less pronounced. However, grains in the 1150 ˚C heat-treated sample were shown to be elongated in the build direction of the samples when compared to the transverse directions; this is likely to lead to non-uniform mechanical properties of the components. Heat treatments also led to the development of some twins within the samples and appeared to strongly promote a crystallographic texture that favoured <110> type directions in the build direction of the specimens.

Applying heat treatments at 1066 ˚C and 1150 ˚C lead to TEM observations of the dissolution of the cellular microstructure and a more homogeneous distribution of solute atoms within the material. APT revealed that segregation to the cell walls in the As-Printed samples may be fairly diffuse, with only slight increases in the measured levels of Mo, Cr, Ni, and Mn; these elements did not appear to show strong segregation behaviour to any particular feature in the APT datasets, which may have contained a cell wall or may have been in close proximity to a cell wall. This demonstrates the benefits of performing APT analysis on multiple volumes

from different areas of an individual specimen, and the insights that can be made by carefully comparing them with one another. Despite the dissolution of the cell structure as a result of heat treatments, APT revealed no change in the atomic distribution of solutes within the matrix. The application of APT did reveal the presence of Co in trace levels within the material and highlights the importance of ensuring that feedstock materials and powders, and printing units are free from impurities when producing components for nuclear applications.

5. Acknowledgements

This project has received funding from the European Union's Horizon 2020 research and innovation programme under the Marie Skłodowska-Curie grant agreement No. 101034329. Recipient of the WINNINGNormandy Program supported by the Normandy Region.

TEM acquisitions on RIO camera have been performed thanks to CATHY project. The European Union and Région Normandie have contributed to the realisation of CATHY project. CATHY is co-funded via the European Regional Development Fund.

Experiments were performed on GENESIS platform instruments supported by the Région Haute-Normandie, the Métropole Rouen Normandie, the CNRS via LABEX EMC^3 and the French National Research Agency as a part of the program “Investissements d’avenir” with the reference ANR-11-EQPX-0020. This work was partially supported by the CNRS Federation IRMA - FR 3095.

6. Appendix

Supplementary Figure 1

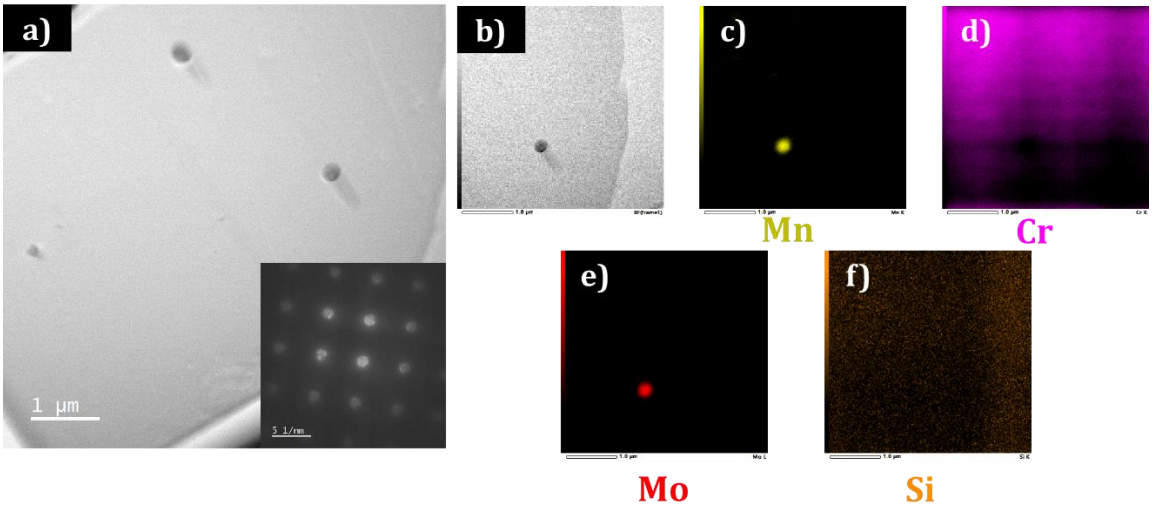

Supplementary Figure 1: (a) and (b) Bright-field images of 1066 ˚C HT sample. STEM-EDS maps of (d) Mn (d) Cr (e) Mo and (f) Si demonstrating that there is no cell structure present. Images were collected on the [001] zone axis with a probe size of 6C and a camera length of 8 cm. The electron current for the EDS maps was 15.2 µA

7. Data Availability

The raw/processed data required to reproduce these findings cannot be shared at this time as the data also forms part of an ongoing study.

8. Bibliography

[1] K.L. Murty, I. Charit, Structural materials for Gen-IV nuclear reactors: Challenges and opportunities, Journal of Nuclear Materials 383 (2008) 189–195. https://doi.org/10.1016/j.jnucmat.2008.08.044.

[2] S. Şahin, M. Übeyli, A Review on the Potential Use of Austenitic Stainless Steels in Nuclear Fusion Reactors, J Fusion Energ 27 (2008) 271–277. https://doi.org/10.1007/s10894-008-9136-3.

[3] F. Dalle, M. Blat-Yrieix, S. Dubiez-Le Goff, C. Cabet, Ph. Dubuisson, Conventional austenitic steels as out-of-core materials for Generation IV nuclear reactors, in: Structural Materials for Generation IV Nuclear Reactors, Elsevier, 2017: pp. 595–633. https://doi.org/10.1016/B978-0-08-100906-2.00017-3.

[4] W.E. Frazier, Metal Additive Manufacturing: A Review, J. of Materi Eng and Perform 23 (2014) 1917–1928. https://doi.org/10.1007/s11665-014-0958-z.

[5] M.K. Thompson, G. Moroni, T. Vaneker, G. Fadel, R.I. Campbell, I. Gibson, A. Bernard, J. Schulz, P. Graf, B. Ahuja, F. Martina, Design for Additive Manufacturing: Trends, opportunities, considerations, and constraints, CIRP Annals 65 (2016) 737–760. https://doi.org/10.1016/j.cirp.2016.05.004.

[6] B.H. Jared, M.A. Aguilo, L.L. Beghini, B.L. Boyce, B.W. Clark, A. Cook, B.J. Kaehr, J. Robbins, Additive manufacturing: Toward holistic design, Scripta Materialia 135 (2017) 141–147. https://doi.org/10.1016/j.scriptamat.2017.02.029.

[7] M.L.M. Sistiaga, S. Nardone, C. Hautfenne, J. van Humbeeck, Effect of heat treatment of 316L stainless steel produced by selective laser melting (SLM), Solid Freeform Fabrication 2016: Proceedings of the 27th Annual International Solid Freeform Fabrication Symposium - An Additive Manufacturing Conference, SFF 2016 (2016) 558–565.

[8] Y.M. Wang, T. Voisin, J.T. McKeown, J. Ye, N.P. Calta, Z. Li, Z. Zeng, Y. Zhang, W. Chen, T.T. Roehling, R.T. Ott, M.K. Santala, P.J. Depond, M.J. Matthews, A.V. Hamza, T. Zhu, Additively manufactured hierarchical stainless steels with high strength and ductility, Nature Mater 17 (2018) 63–71. https://doi.org/10.1038/nmat5021.

[9] Y. Kok, X.P. Tan, P. Wang, M.L.S. Nai, N.H. Loh, E. Liu, S.B. Tor, Anisotropy and heterogeneity of microstructure and mechanical properties in metal additive manufacturing: A critical review, Materials & Design 139 (2018) 565–586. https://doi.org/10.1016/j.matdes.2017.11.021.

[10] A.-H. Puichaud, C. Flament, A. Chniouel, F. Lomello, E. Rouesne, P.-F. Giroux, H. Maskrot, F. Schuster, J.-L. Béchade, Microstructure and mechanical properties relationship of additively manufactured 316L stainless steel by selective laser melting, EPJ Nuclear Sciences & Technologies 5 (2019) 23. https://doi.org/10.1051/epjn/2019051.

[11] B. Blinn, F. Krebs, M. Ley, R. Teutsch, T. Beck, Determination of the influence of a stress-relief heat treatment and additively manufactured surface on the fatigue behavior of selectively laser melted AISI 316L by using efficient short-time procedures ☆, International Journal of Fatigue 131 (2020) 105301. https://doi.org/10.1016/j.ijfatigue.2019.105301.

[12] D. Kong, C. Dong, S. Wei, X. Ni, L. Zhang, R. Li, L. Wang, C. Man, X. Li, About metastable cellular structure in additively manufactured austenitic stainless steels, Additive Manufacturing 38 (2021). https://doi.org/10.1016/j.addma.2020.101804.

[13] L.S. Aota, P. Bajaj, K.D. Zilnyk, E.A. Jägle, D. Ponge, H.R.Z. Sandim, D. Raabe, Recrystallization kinetics, mechanisms, and topology in alloys processed by laser powder-bed fusion: AISI 316L stainless steel as example, Materialia 20 (2021) 101236. https://doi.org/10.1016/j.mtla.2021.101236.

[14] S. Gao, Z. Hu, M. Duchamp, P.S.S.R. Krishnan, S. Tekumalla, X. Song, M. Seita, Recrystallization-based grain boundary engineering of 316L stainless steel produced via selective laser melting, Acta Materialia 200 (2020) 366–377. https://doi.org/10.1016/j.actamat.2020.09.015.

[15] F.C. Pinto, L.S. Aota, I.R. Souza Filho, D. Raabe, H.R.Z. Sandim, Recrystallization in non-conventional microstructures of 316L stainless steel produced via laser powder-bed fusion: effect of particle coarsening kinetics, J Mater Sci 57 (2022) 9576–9598. https://doi.org/10.1007/s10853-021-06859-1.
[16] O. Andreau, I. Koutiri, P. Peyre, J.D. Penot, N. Saintier, E. Pessard, T. De Terris, C. Dupuy, T. Baudin, Texture control of 316L parts by modulation of the melt pool morphology in selective laser melting, Journal of Materials Processing Technology 264 (2019) 21–31. https://doi.org/10.1016/j.jmatprotec.2018.08.049.
[17] D. Ma, A.D. Stoica, Z. Wang, A.M. Beese, Crystallographic texture in an additively manufactured nickel-base superalloy, Materials Science and Engineering: A 684 (2017) 47–53. https://doi.org/10.1016/j.msea.2016.12.028.
[18] J.M. Jeon, J.M. Park, J.-H. Yu, J.G. Kim, Y. Seong, S.H. Park, H.S. Kim, Effects of microstructure and internal defects on mechanical anisotropy and asymmetry of selective laser-melted 316L austenitic stainless steel, Materials Science and Engineering: A 763 (2019) 138152. https://doi.org/10.1016/j.msea.2019.138152.
[19] U. Scipioni Bertoli, B.E. MacDonald, J.M. Schoenung, Stability of cellular microstructure in laser powder bed fusion of 316L stainless steel, Materials Science and Engineering: A 739 (2019) 109–117. https://doi.org/10.1016/j.msea.2018.10.051.
[20] M. Kazemipour, M. Mohammadi, E. Mfoumou, A.M. Nasiri, Microstructure and Corrosion Characteristics of Selective Laser-Melted 316L Stainless Steel: The Impact of Process-Induced Porosities, JOM 71 (2019) 3230–3240. https://doi.org/10.1007/s11837-019-03647-w.
[21] T. Niendorf, S. Leuders, A. Riemer, H.A. Richard, T. Tröster, D. Schwarze, Highly Anisotropic Steel Processed by Selective Laser Melting, Metall Mater Trans B 44 (2013) 794–796. https://doi.org/10.1007/s11663-013-9875-z.
[22] T.B. Britton, J. Jiang, Y. Guo, A. Vilalta-Clemente, D. Wallis, L.N. Hansen, A. Winkelmann, A.J. Wilkinson, Tutorial: Crystal orientations and EBSD — Or which way is up?, Materials Characterization 117 (2016) 113–126. https://doi.org/10.1016/j.matchar.2016.04.008.
[23] A. Yadollahi, N. Shamsaei, S.M. Thompson, D.W. Seely, Effects of process time interval and heat treatment on the mechanical and microstructural properties of direct laser deposited 316L stainless steel, Materials Science and Engineering A 644 (2015) 171–183. https://doi.org/10.1016/j.msea.2015.07.056.
[24] L.E. Murr, A Metallographic Review of 3D Printing/Additive Manufacturing of Metal and Alloy Products and Components, Metallogr. Microstruct. Anal. 7 (2018) 103–132. https://doi.org/10.1007/s13632-018-0433-6.
[25] R.J. Williams, F. Vecchiato, J. Kelleher, M.R. Wenman, P.A. Hooper, C.M. Davies, Effects of heat treatment on residual stresses in the laser powder bed fusion of 316L stainless steel: Finite element predictions and neutron diffraction measurements, Journal of Manufacturing Processes 57 (2020) 641–653. https://doi.org/10.1016/j.jmapro.2020.07.023.
[26] Q. Zeng, K. Gan, Y. Wang, Effect of Heat Treatment on Microstructures and Mechanical Behaviors of 316L Stainless Steels Synthesized by Selective Laser Melting, J. of Materi Eng and Perform 30 (2021) 409–422. https://doi.org/10.1007/s11665-020-05330-7.
[27] L.A. Giannuzzi, J.L. Drown, S.R. Brown, R.B. Irwin, F.A. Stevie, Applications of the FIB lift-out technique for TEM specimen preparation, Microscopy Research and Technique 41 (1998) 285–290. https://doi.org/10.1002/(SICI)1097-0029(19980515)41:4<285::AID-JEMT1>3.0.CO;2-Q.
[28] D.J. Larson, D.T. Foord, A.K. Petford-Long, T.C. Anthony, I.M. Rozdilsky, A. Cerezo, G.D.W. Smith, Focused ion-beam milling for field-ion specimen preparation: Preliminary investigations, Ultramicroscopy 75 (1998) 147–159. https://doi.org/10.1016/S0304-3991(98)00058-8.
[29] M.K. Miller, K.F. Russell, G.B. Thompson, Strategies for fabricating atom probe specimens with a dual beam FIB, Ultramicroscopy 102 (2005) 287–298. https://doi.org/10.1016/j.ultramic.2004.10.011.

[30] M.K. Miller, K.F. Russell, Atom probe specimen preparation with a dual beam SEM/FIB miller, Ultramicroscopy 107 (2007) 761–766. https://doi.org/10.1016/j.ultramic.2007.02.023.
[31] K. Thompson, D. Lawrence, D.J. Larson, J.D. Olson, T.F. Kelly, B. Gorman, In situ site-specific specimen preparation for atom probe tomography, Ultramicroscopy 107 (2007) 131–139. https://doi.org/10.1016/j.ultramic.2006.06.008.
[32] S. Rouland, B. Radiguet, P. Pareige, Investigating radiation-induced segregation on intragranular defects in a 316L(N), Journal of Nuclear Materials 557 (2021) 153216. https://doi.org/10.1016/j.jnucmat.2021.153216.
[33] A.J. London, Quantifying Uncertainty from Mass-Peak Overlaps in Atom Probe Microscopy, Microscopy and Microanalysis (2019) 1–11. https://doi.org/10.1017/S1431927618016276.
[34] A.J. London, AtomProbeLab, (2019) https://sourceforge.net/projects/atomprobelab/. https://sourceforge.net/projects/atomprobelab/.
[35] D. Kong, X. Ni, C. Dong, L. Zhang, C. Man, J. Yao, K. Xiao, X. Li, Heat treatment effect on the microstructure and corrosion behavior of 316L stainless steel fabricated by selective laser melting for proton exchange membrane fuel cells, Electrochimica Acta 276 (2018) 293–303. https://doi.org/10.1016/j.electacta.2018.04.188.
[36] R. Casati, J. Lemke, M. Vedani, Microstructure and Fracture Behavior of 316L Austenitic Stainless Steel Produced by Selective Laser Melting, Journal of Materials Science and Technology 32 (2016) 738–744. https://doi.org/10.1016/j.jmst.2016.06.016.
[37] B.P. Eftink, J.S. Weaver, J.A. Valdez, V. Livescu, D. Chen, Y. Wang, C. Knapp, N.A. Mara, S.A. Maloy, G.T. Gray, Proton irradiation and characterization of additively manufactured 304L stainless steels, Journal of Nuclear Materials 531 (2020). https://doi.org/10.1016/j.jnucmat.2020.152007.
[38] M. Godec, S. Zaefferer, B. Podgornik, M. Šinko, E. Tchernychova, Quantitative multiscale correlative microstructure analysis of additive manufacturing of stainless steel 316L processed by selective laser melting, Materials Characterization 160 (2020). https://doi.org/10.1016/j.matchar.2019.110074.
[39] O.O. Salman, C. Gammer, A.K. Chaubey, J. Eckert, S. Scudino, Effect of heat treatment on microstructure and mechanical properties of 316L steel synthesized by selective laser melting, Materials Science and Engineering A 748 (2019) 205–212. https://doi.org/10.1016/j.msea.2019.01.110.
[40] A.B. Kale, J. Singh, B.-K. Kim, D.-I. Kim, S.-H. Choi, Effect of initial microstructure on the deformation heterogeneities of 316L stainless steels fabricated by selective laser melting processing, Journal of Materials Research and Technology 9 (2020) 8867–8883. https://doi.org/10.1016/j.jmrt.2020.06.015.
[41] C. Qiu, M.A. Kindi, A.S. Aladawi, I.A. Hatmi, A comprehensive study on microstructure and tensile behaviour of a selectively laser melted stainless steel, Sci Rep 8 (2018) 7785. https://doi.org/10.1038/s41598-018-26136-7.
[42] S. Bahl, S. Mishra, K.U. Yazar, I.R. Kola, K. Chatterjee, S. Suwas, Non-equilibrium microstructure, crystallographic texture and morphological texture synergistically result in unusual mechanical properties of 3D printed 316L stainless steel, Additive Manufacturing 28 (2019) 65–77. https://doi.org/10.1016/j.addma.2019.04.016.
[43] J.A. Evans, S.A. Anderson, E.J. Faierson, D. Perez-Nunez, S.M. McDeavitt, Anisotropic Radiation-Induced Changes in Type 316L Stainless Steel Rods Built by Laser Additive Manufacturing, Nuclear Technology 205 (2019) 563–581. https://doi.org/10.1080/00295450.2018.1502001.
[44] M. Loyer-Prost, A.H. Puichaud, C. Flament, E. Rouesne, J.L. Béchade, Impact of intragranular misorientation on void swelling and inter-granular cavities after ion irradiation in standard and additive manufacturing 316L austenitic steels, Journal of Nuclear Materials 573 (2023). https://doi.org/10.1016/j.jnucmat.2022.154102.
[45] J. Nguejio, M. Mokhtari, E. Paccou, E. Baustert, L. Khalij, E. Hug, P. Bernard, S. Boileau, C. Keller, Combined effect of a spread powder particle size distribution, surface machining and stress-relief heat treatment on microstructure, tensile and fatigue

properties of 316L steel manufactured by laser powder bed fusion, The International Journal of Advanced Manufacturing Technology (2023). https://doi.org/10.1007/s00170-023-11008-w.
[46] M.S. Pham, B. Dovgyy, P.A. Hooper, C.M. Gourlay, A. Piglione, The role of side-branching in microstructure development in laser powder-bed fusion, Nature Communications 11 (2020). https://doi.org/10.1038/s41467-020-14453-3.
[47] H. Qu, J. Li, F. Zhang, J. Bai, Anisotropic cellular structure and texture microstructure of 316L stainless steel fabricated by selective laser melting via rotation scanning strategy, Materials and Design 215 (2022). https://doi.org/10.1016/j.matdes.2022.110454.
[48] M. Song, M. Wang, X. Lou, R.B. Rebak, G.S. Was, Radiation damage and irradiation-assisted stress corrosion cracking of additively manufactured 316L stainless steels, Journal of Nuclear Materials 513 (2019) 33–44. https://doi.org/10.1016/j.jnucmat.2018.10.044.
[49] Z. Sun, X. Tan, S.B. Tor, C.K. Chua, Simultaneously enhanced strength and ductility for 3D-printed stainless steel 316L by selective laser melting, NPG Asia Mater 10 (2018) 127–136. https://doi.org/10.1038/s41427-018-0018-5.
[50] Z. Duan, C. Man, C. Dong, Z. Cui, D. Kong, L. wang, X. Wang, Pitting behavior of SLM 316L stainless steel exposed to chloride environments with different aggressiveness: Pitting mechanism induced by gas pores, Corrosion Science 167 (2020) 108520. https://doi.org/10.1016/j.corsci.2020.108520.
[51] Y. Song, Q. Sun, K. Guo, X. Wang, J. Liu, J. Sun, Effect of scanning strategies on the microstructure and mechanical behavior of 316L stainless steel fabricated by selective laser melting, Materials Science and Engineering: A 793 (2020) 139879. https://doi.org/10.1016/j.msea.2020.139879.
[52] Y. Zhong, L.-E. Rännar, L. Liu, A. Koptyug, S. Wikman, J. Olsen, D. Cui, Z. Shen, Additive manufacturing of 316L stainless steel by electron beam melting for nuclear fusion applications, Journal of Nuclear Materials 486 (2017) 234–245. https://doi.org/10.1016/j.jnucmat.2016.12.042.
[53] J. Olsén, Z. Shen, L. Liu, A. Koptyug, L.-E. Rännar, Micro- and macro-structural heterogeneities in 316L stainless steel prepared by electron-beam melting, Materials Characterization 141 (2018) 1–7. https://doi.org/10.1016/j.matchar.2018.04.026.
[54] N. Nadammal, S. Cabeza, T. Mishurova, T. Thiede, A. Kromm, C. Seyfert, L. Farahbod, C. Haberland, J.A. Schneider, P.D. Portella, G. Bruno, Effect of hatch length on the development of microstructure, texture and residual stresses in selective laser melted superalloy Inconel 718, Materials and Design 134 (2017) 139–150. https://doi.org/10.1016/j.matdes.2017.08.049.
[55] G. Meric de Bellefon, K.M. Bertsch, M.R. Chancey, Y.Q. Wang, D.J. Thoma, Influence of solidification structures on radiation-induced swelling in an additively-manufactured austenitic stainless steel, Journal of Nuclear Materials 523 (2019) 291–298. https://doi.org/10.1016/j.jnucmat.2019.06.012.
[56] S. Chen, G. Ma, G. Wu, A. Godfrey, T. Huang, X. Huang, Strengthening mechanisms in selective laser melted 316L stainless steel, Materials Science and Engineering A 832 (2022). https://doi.org/10.1016/j.msea.2021.142434.
[57] T.S. Byun, B.E. Garrison, M.R. McAlister, X. Chen, M.N. Gussev, T.G. Lach, A.L. Coq, K. Linton, C.B. Joslin, J.K. Carver, F.A. List, R.R. Dehoff, K.A. Terrani, Mechanical behavior of additively manufactured and wrought 316L stainless steels before and after neutron irradiation, Journal of Nuclear Materials 548 (2021) 152849. https://doi.org/10.1016/j.jnucmat.2021.152849.
[58] S.-H. Sun, K. Hagihara, T. Nakano, Effect of scanning strategy on texture formation in Ni-25 at.%Mo alloys fabricated by selective laser melting, Materials & Design 140 (2018) 307–316. https://doi.org/10.1016/j.matdes.2017.11.060.
[59] V.B. Vukkum, R.K. Gupta, Review on corrosion performance of laser powder-bed fusion printed 316L stainless steel: Effect of processing parameters, manufacturing defects, post-processing, feedstock, and microstructure, Materials and Design 221 (2022) 110874. https://doi.org/10.1016/j.matdes.2022.110874.

[60] T. DebRoy, H.L. Wei, J.S. Zuback, T. Mukherjee, J.W. Elmer, J.O. Milewski, A.M. Beese, A. Wilson-Heid, A. De, W. Zhang, Additive manufacturing of metallic components – Process, structure and properties, Progress in Materials Science 92 (2018) 112–224. https://doi.org/10.1016/j.pmatsci.2017.10.001.
[61] K.M. Bertsch, G. Meric de Bellefon, B. Kuehl, D.J. Thoma, Origin of dislocation structures in an additively manufactured austenitic stainless steel 316L, Acta Materialia 199 (2020) 19–33. https://doi.org/10.1016/j.actamat.2020.07.063.
[62] A.J. Birnbaum, J.C. Steuben, E.J. Barrick, A.P. Iliopoulos, J.G. Michopoulos, Intrinsic strain aging, Σ3 boundaries, and origins of cellular substructure in additively manufactured 316L, Additive Manufacturing 29 (2019). https://doi.org/10.1016/j.addma.2019.100784.
[63] P. Krakhmalev, G. Fredriksson, K. Svensson, I. Yadroitsev, I. Yadroitsava, M. Thuvander, R. Peng, Microstructure, solidification texture, and thermal stability of 316 L stainless steel manufactured by laser powder bed fusion, Metals 8 (2018). https://doi.org/10.3390/met8080643.
[64] L. Liu, Q. Ding, Y. Zhong, J. Zou, J. Wu, Y.-L. Chiu, J. Li, Z. Zhang, Q. Yu, Z. Shen, Dislocation network in additive manufactured steel breaks strength–ductility trade-off, Materials Today 21 (2018) 354–361. https://doi.org/10.1016/j.mattod.2017.11.004.
[65] Y.T. Tang, C. Panwisawas, B.M. Jenkins, J. Liu, Z. Shen, E. Salvati, Y. Gong, J.N. Ghoussoub, S. Michalik, B. Roebuck, P.A.J. Bagot, S. Lozano-Perez, C.R.M. Grovenor, M.P. Moody, A.M. Korsunsky, D.M. Collins, R.C. Reed, Multi-length-scale study on the heat treatment response to supersaturated nickel-based superalloys: Precipitation reactions and incipient recrystallisation, Additive Manufacturing 62 (2023). https://doi.org/10.1016/j.addma.2023.103389.
[66] A. International Atomic Energy Agency, Radiation protection aspects of design for nuclear power plants, International Atomic Energy Agency, Vienna, 2005. https://www.iaea.org/publications/7293/radiation-protection-aspects-of-design-for-nuclear-power-plants.
[67] T.T. Tsong, G. Kellogg, Direct observation of the directional walk of single adatoms and the adatom polarizability, Physical Review B 12 (1975) 1343–1353. https://doi.org/10.1103/PhysRevB.12.1343.
[68] J.M. Hyde, M.G. Burke, B. Gault, D.W. Saxey, P.D. Styman, K.B. Wilford, T.J. Williams, Atom probe tomography of reactor pressure vessel steels: an analysis of data integrity, Ultramicroscopy 111 (2011) 676–682. https://doi.org/10.1016/j.ultramic.2010.12.033.